Synchronization and Coexistence in Quantum Networks

IVAN A. BURENKOV[1,2,*], ALEXANDRA SEMIONOVA[2], HALA[2], THOMAS GERRITS[2], ANOUAR RAHMOUNI[2], DJ ANAND[2], YA-SHIAN LI-BABOUD[2], OLIVER SLATTERY[2], ABDELLA BATTOU[2], AND SERGEY V. POLYAKOV[2,3]

[1]*Joint Quantum Institute & University of Maryland, College Park, MD 20742, USA*
[2]*National Institute of Standards and Technology, Gaithersburg, Maryland 20899, USA*
[3]*Department of Physics, University of Maryland, College Park, MD 20742, USA*
[*]*ivan.burenkov@gmail.com*
https://iburenkov.com

Abstract: We investigate the coexistence of clock synchronization protocols with quantum signals in a common single-mode optical fiber. By measuring optical noise between 1500 nm to 1620 nm we demonstrate a potential for up to 100 quantum, 100 GHz wide channels coexisting with the classical synchronization signals. Both "White Rabbit" and pulsed laser-based synchronization protocols were characterized and compared. We establish a theoretical limit of the fiber link length for coexisting quantum and classical channels. The maximal fiber length is below approximately 100 km for off-the-shelf optical transceivers and can be significantly improved by taking advantage of quantum receivers.

1. Introduction

Synchronization of quantum network nodes is essential for the successful realization of quantum communication protocols including quantum key distribution [1] and entanglement distribution [2–4] as well as entanglement swapping [5,6]. Because many quantum communication protocols were demonstrated using fiber spools to simulate a network [7–12], the quantum nodes are co-located and the long-distance synchronization has limited exposure to environmental variabilities. Furthermore, practical deployment of these protocols using remote network nodes requires precise time synchronization. Recently, entanglement distribution was demonstrated in a dedicated quantum network using the Global Positioning System (GPS) based protocol for time-synchronization [13]. The nanosecond-scale timing jitter was sufficient to verify entanglement distribution in post-selection, and the authors found that the fidelity can be significantly improved with lower time jitter enabling a shorter coincidence window [14]. Other techniques, such as the White Rabbit (WR) precision time protocol (PTP) [15, 16] , which has been standardized in the high-accuracy PTP (HA-PTP) [17], can be used to achieve picosecond scale timing distributed via a fiber-optic network [18]. All such techniques rely on classical communication. Using a secondary optical fiber for time synchronization is often impractical [19] and in some circumstances can be prohibitive. Because the optical power (photon rate) at the receiver of classical channels are 7 to 12 orders of magnitude higher than that of quantum channels, classical optical pulses can generate significant noise in coexisting quantum channels. This effect is significantly more pronounced in long-distance links, because the launching power in classical channels is significantly higher than that required at the receiver to mitigate fiber losses. Despite the challenges, the coexistence was demonstrated in a single mode common fiber for a limited case of classical channels with quantum key distribution channels that use weak coherent

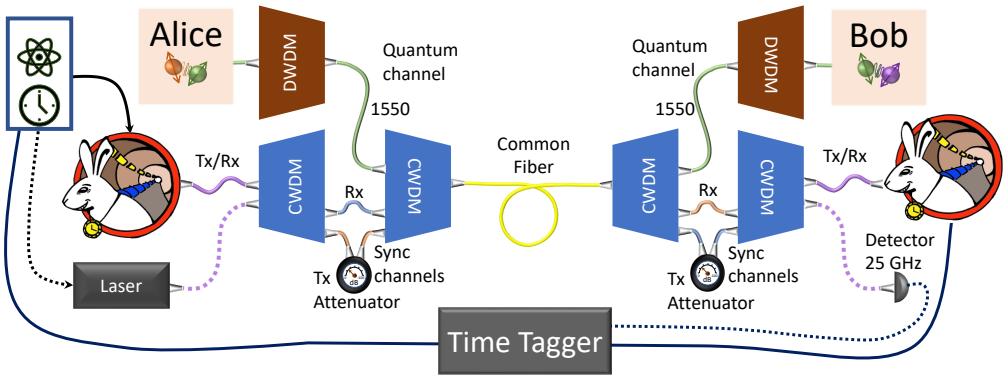

Fig. 1. Experimental setup. The yellow loop represents the common optical fiber spool used for the measurements. The common fiber is connected to a CWDM that multiplexes and demultiplexes of quantum and classical channels at each end. The bandwidth intended for the quantum use is further divided into narrow DWDM channels. Another pair of CWDMs is placed before the classical transmitters to remove out-of-band noise generated by the transmitter's source. A pair of variable attenuators are introduced in transmission channels between the CWDMs to control the input power of classical signals launched into the common fiber. Noise measurements are performed with an superconducting nanowire single-photon detector (SNSPD) in the 1547.72 nm DWDM channel on both Alice and Bob sides. Timing jitter is measured between the 10 MHz rubidium clock driving the WR leader switch (grandmaster clock) or the pulsed laser and the WR follower switch (boundary clock) or the fast InGaAs detector correspondingly. See [26] for WR logo copyright information.

pulses [20–22]. In addition, a limited experimental demonstration of coexistence for entangled states distribution has been reported in conference proceedings [23,24]. However, the coexistence of classical and quantum channels was not studied in a systematic way.

In this work, we build and characterize the two-node time-synchronized quantum network testbed (TSQNT) and test coexistence of quantum links with classical synchronization protocols in a common (SMF28) single-mode optical fiber, here the only classical signals in the fiber are the signals produced by WR synchronization protocol. We employ WR [25] and a pulsed-laser-based synchronization protocols for this study. We use 1270 nm, 1310 nm, 1330 nm, and 1490 nm classical bi-directional transceivers and a 1310 nm pulsed laser.

In our study, we offer a heuristic model for background generation in long fiber links. We make systematic background measurements in one of the dense wavelength division multiplexing (DWDM) channels (1547.72 nm, 100 GHz bandwidth), then we estimate the background in the range from 1500 nm to 1620 nm. Separately, we verify and characterize the synchronization quality between the two distant nodes.

2. Experimental setup

The two-node TSQNT is shown in Fig. 1 and includes both quantum and classical components. Quantum nodes, shown as Alice and Bob, utilized narrow (100 GHz) DWDM channels ranging from 1500 nm to 1620 nm. Clock synchronization is implemented with (a) a pair of WR switches, configured as a grandmaster (GM) and a boundary clock (BC), with commercial transceivers using pair of wavelengths to transmit (Tx) and receive (Rx) data: 1310 nm and 1490 nm or 1270 nm and 1330 nm, and (b) a $\lesssim$100 ps pulsed laser at 1310 nm and 10 MHz repetition rate.

Because classical light sources may have a broad background that extends to the wavelength

range of quantum channels, the fiber from the classical transceiver is sent through a pair of commercial coarse wave division multiplexing (CWDM) modules at each end of the common optical fiber. The WR or laser signals are demultiplexed and then only active WR wavelength pairs or pulsed laser wavelengths are connected to another commercial CWDM and multiplexed into the common fiber. In that way, the broad background that can be generated by transmitters is filtered out. According to specifications, the adjacent CWDM channels are suppressed by more than 30 dB and for not-adjacent channels by at least 40 dB. The range of wavelengths from 1500 nm to 1620 nm is intended for quantum use. In our setup, those wavelengths are accessible through the six 20 nm wide CWDM channels (1510 nm, 1530 nm, 1550 nm, 1570 nm, 1590 nm, and 1610 nm). We use a commercial DWDM to extract a single quantum channel where the measurements are made (at 1547.72 nm with 100 GHz bandwidth) for both Alice and Bob sites. Further, we use a spectrometer for a separate measurement of background light in each of the six CWDM channels to quantify the amount of background noise in other quantum communication channels. We measure background photon rates at both the Alice and Bob nodes of the quantum channel. Noise due to back-scattering (BS) propagates in the opposite direction to the transmitted signal, whereas noise due to forward-scattering (FS) co-propagates with the transmitted signal.

To verify synchronization, the WR leader or the pulsed laser are driven by a stable rubidium clock at 10 MHz at the Alice node. Then the 10 MHz clock signals from Bob and Alice nodes are compared. In case of the WR switches, the 10 MHz outputs from the GM clock and the BC were compared. In the case of a pulsed laser, the rubidium clock signal was compared to the fast (25 GHz bandwidth) InGaAs detector output. We used a low-jitter (1.5 ps RMS) time-tagger to quantify the timing jitter of the two synchronization distribution arrangements.

We make measurements for a set of 4 fiber spools with lengths: 1 km, 6 km, 12 km, and 25 km. Variable attenuators in transmission (Tx) channels connecting inner and outer CWDMs are used to attenuate input classical signal power in the common optical fiber channel.

3. Results and discussion

3.1. A heuristic model for noise generation in a common optical fiber channel

Consider a narrowband classical signal at wavelength λ_s and a launching power P_{in} (measured in photons per second) propagating in a fiber. After propagation distance l the signal power will decrease due to attenuation:

$$P_{\text{signal}}(l) = P_{\text{s}}(l) = P_{\text{in}} e^{-\alpha_{\text{s}} l}, \tag{1}$$

where α_{s} is the attenuation at a signal wavelength λ_{s}. Formally, $\alpha_{\text{s}} = f(\lambda_{\text{s}})$ in (1), however, because both classical and quantum channels are spectrally narrow (typically, ≤ 1 nm), we assume that attenuation is constant in each channel. The average number of back-propagating noise photons at the transmitter end generated in a quantum channel at λ_{n} with bandwidth $\mathrm{d}\lambda_{\text{n}}$ by the signal due to inelastic scattering in any short section of the fiber $[l,\ l + \mathrm{d}l]$, where $\mathrm{d}l \to 0$ is:

$$\rho^{\text{BS}}(l) = \beta^{\text{BS}}_{\lambda_{\text{s}},\lambda_{\text{n}}} e^{-\alpha_{\text{n}} l} P_{\text{s}}(l) \mathrm{d}l \mathrm{d}\lambda_{\text{n}},$$

where α_{n} is the attenuation constant at wavelength λ_{n}, the exponential factor $e^{-\alpha_{\text{n}} l}$ describes losses in the fiber for the noise photons as they back-propagate to the fiber input, and $\beta^{\text{BS}}_{\lambda_{\text{s}},\lambda_{\text{n}}}$ is a coefficient relating signal photon rate at λ_{s} to the noise photon rate at λ_{n} because of inelastic backscattering in a fiber of a unit length and bandwidth. By integrating this expression over the fiber length, we can obtain the average number of noise photons back-scattered into a channel with bandwidth $\mathrm{d}\lambda_{\text{n}}$ from the entire fiber link of length L for a given launching signal power P_{in}:

$$P_{\text{BS}}(L) = \frac{(1 - e^{-(\alpha_{\text{s}} + \alpha_{\text{n}})L}) \beta^{\text{BS}}_{\lambda_{\text{s}},\lambda_{\text{n}}} \mathrm{d}\lambda_{\text{n}} P_{\text{in}}}{\alpha_{\text{s}} + \alpha_{\text{n}}}. \tag{2}$$

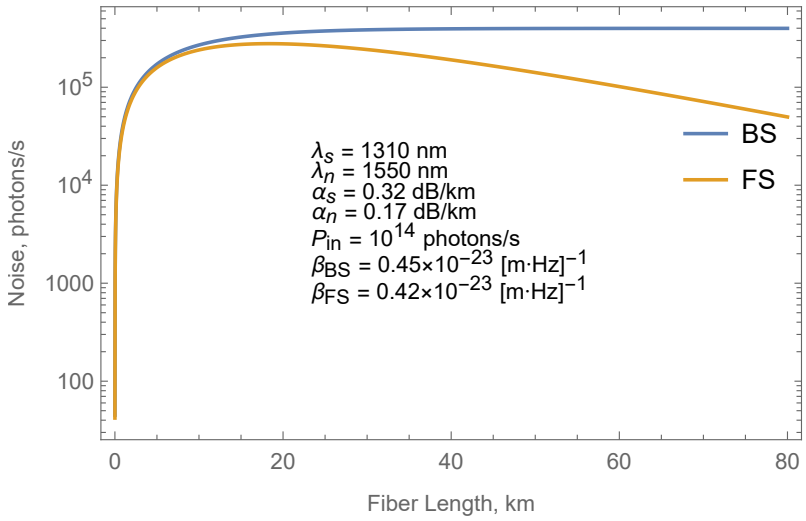

Fig. 2. Theoretical dependencies of the BS and FS noise generated in a single DWDM channel (with 100 GHz bandwidth) at $\lambda_n = 1550$ nm ($\alpha_n = 0.17$ dB/km) by a narrowband signal at $\lambda_s = 1310$ nm ($\alpha_s = 0.32$ dB/km) as a function of a single mode optical fiber length and fixed launching power $P_{in} = 10^{14}$ photons per second.

Similarly, the average number of co-propagating noise photons at the receiver end generated by the signal because of inelastic scattering in any short section of the fiber $[l,\ l + dl]$ into a quantum channel at wavelength λ_n is:

$$\rho^{FS}(l) = \beta^{FS}_{\lambda_s,\lambda_n} e^{-\alpha_n(L-l)} P_s(l) dl d\lambda_n,$$

where $\beta^{FS}_{\lambda_s,\lambda_n}$ is a coefficient relating the signal photon rate at λ_s to the noise photon rate at λ_n because of inelastic forward-scattering (FS) in a fiber of a unit length. The average number of noise forward-scattered photons in the entire link of the length L for a given launching signal power P_{in} is:

$$P_{FS}(L) = \frac{(e^{-\alpha_n L} - e^{-\alpha_s L})\beta^{FS}_{\lambda_s,\lambda_n} d\lambda_n P_{in}}{\alpha_s - \alpha_n}. \quad (3)$$

This model of backward and forward scattering relates the expected background noise to the total length of the optical fiber network links and transceiver launching power via a pair of parameters, $\beta^{BS}_{\lambda_s,\lambda_n}$ and $\beta^{FS}_{\lambda_s,\lambda_n}$. Therefore, by quantifying $\beta^{BS}_{\lambda_s,\lambda_n}$ and $\beta^{FS}_{\lambda_s,\lambda_n}$, background noise in quantum links that are coexisting with classical links can be predicted. For example, Fig. 2 shows a theoretical dependence of the BS and FS noise generated in a narrowband channel at $\lambda_n = 1550$ nm ($\alpha_n = 0.17$ dB/km) by a narrowband signal at $\lambda_s = 1310$ nm ($\alpha_s = 0.32$ dB/km) in dependence on the common optical fiber length for a fixed launching power $P_{in} = 10^{14}$ photons per second. The noise conversion constants $\beta^{BS}_{\lambda_s,\lambda_n}$ and $\beta^{FS}_{\lambda_s,\lambda_n}$ are set to close to the values extracted from the fits of experimental data, bandwidth $d\lambda_n$ corresponds to the bandwidth of a single DWDM channel (100 GHz). The dependencies demonstrate similar behaviors for a short fiber length $L < 10$ km. In longer links, the BS saturates to a constant value $P_{in}\beta^{BS}_{\lambda_s,\lambda_n}/(\alpha_s + \alpha_n)$. This is because the back-scattered light generated further away from the measurement node is strongly attenuated. In contrast, the FS decreases with the link length. This decrease is most evident for links $L \geq 20$ km because both the signal and co-propagating noise are attenuated; less noise is generated further away from the source.

The above theoretical model does not account for additional terminal losses (IL) at the fiber link input and output terminals. These losses can be extracted from a set of simple measurements.

Thus, measured background noise can be related to generated background noise:

$$\begin{cases} P^{\mathrm{AB}}_{\mathrm{BS,exp}}(L) = P_{\mathrm{BS}}(L)\eta^{\mathrm{A}}_{\lambda_{\mathrm{s}}}\eta^{\mathrm{A}}_{\lambda_{\mathrm{n}}} \\ P^{\mathrm{BA}}_{\mathrm{BS,exp}}(L) = P_{\mathrm{BS}}(L)\eta^{\mathrm{B}}_{\lambda_{\mathrm{s}}}\eta^{\mathrm{B}}_{\lambda_{\mathrm{n}}} \\ P^{\mathrm{AB}}_{\mathrm{FS,exp}}(L) = P_{\mathrm{FS}}(L)\eta^{\mathrm{A}}_{\lambda_{\mathrm{s}}}\eta^{\mathrm{B}}_{\lambda_{\mathrm{n}}} \\ P^{\mathrm{BA}}_{\mathrm{FS,exp}}(L) = P_{\mathrm{FS}}(L)\eta^{\mathrm{B}}_{\lambda_{\mathrm{s}}}\eta^{\mathrm{A}}_{\lambda_{\mathrm{n}}}, \end{cases} \tag{4}$$

where "A" and "B" label Alice's and Bob's terminals, respectively. $P^{\mathrm{AB}}_{\mathrm{BS,exp}}(L)$ is the experimentally measured average number of noise photons back-scattered from the entire fiber link of length L where top indexes denote input and output terminal: in this example "A" used as a signal input and "B" as the output. Thus, the transmissivity of the whole link is:

$$\begin{cases} \eta^{\mathrm{total}}_{\lambda_{\mathrm{s}}} = \eta^{\mathrm{A}}_{\lambda_{\mathrm{s}}}\eta^{\mathrm{internal}}_{\lambda_{\mathrm{s}}}\eta^{\mathrm{B}}_{\lambda_{\mathrm{s}}} \\ \eta^{\mathrm{total}}_{\lambda_{\mathrm{n}}} = \eta^{\mathrm{A}}_{\lambda_{\mathrm{n}}}\eta^{\mathrm{internal}}_{\lambda_{\mathrm{n}}}\eta^{\mathrm{B}}_{\lambda_{\mathrm{n}}}, \end{cases} \tag{5}$$

where $\eta^{\mathrm{total}}_{\lambda_{\mathrm{x}}}$ is the total transmissivity of the link measured in the experiment as the ratio of output and input optical powers, and $\eta^{\mathrm{internal}}_{\lambda_{\mathrm{x}}} = e^{-\alpha_{\lambda_{\mathrm{x}}}L}$ is the transmissivity of the fiber link at wavelength "λ_{x}". The theoretical transmissivity is based on fused silica attenuation constants at corresponding wavelengths (for the values used in this work, see Table 1). Both raw experimental noise counts rates and corrected for fiber link insetion losses at the fiber terminals (η^{A} and η^{B}) count rates ($P_{\mathrm{BS}}(L)$ and $P_{\mathrm{FS}}(L)$) in the 1547.72 nm DWDM channel are shown in Fig. 4 along with model curves (2) and (3) plotted for coefficients $\beta^{\mathrm{BS}}_{\lambda_{\mathrm{s}},\lambda_{\mathrm{n}}}$ and $\beta^{\mathrm{FS}}_{\lambda_{\mathrm{s}},\lambda_{\mathrm{n}}}$ extracted from (4) using data obtained for the 25 km link.

In designing practical links, the output signal power is set given the sensitivity of the available receiver. Therefore, a formula for background noise based on the output signal power (rather than the launching power) is useful. These expressions can be easily obtained from equations (2) and (3), by replacing the launching power with the received power $P_{\mathrm{in}} = P_{\mathrm{out}}e^{\alpha_{\mathrm{s}}L}$. Then the expressions for noise in BS and FS channels can be written as:

$$P_{\mathrm{BS}}(L) = \frac{(e^{\alpha_{\mathrm{s}}L} - e^{-\alpha_{\mathrm{n}}L})\beta^{\mathrm{BS}}_{\lambda_{\mathrm{s}},\lambda_{\mathrm{n}}}P_{\mathrm{out}}}{\alpha_{\mathrm{s}} + \alpha_{\mathrm{n}}}, \qquad P_{\mathrm{FS}}(L) = \frac{(e^{(\alpha_{\mathrm{s}}-\alpha_{\mathrm{n}})L} - 1)\beta^{\mathrm{FS}}_{\lambda_{\mathrm{s}},\lambda_{\mathrm{n}}}P_{\mathrm{out}}}{\alpha_{\mathrm{s}} - \alpha_{\mathrm{n}}}. \tag{6}$$

3.2. Background noise as a function of the fiber length and synchronization signal power

The noise photon rate is corrected for the superconducting nanowire single-photon detector (SNSPD) detection efficiency of 0.957(5) [27] for polarization that maximazes the detection efficiency and 0.495(5) for orthogonal polarization (certain orientation of the superconducting nanowire meander results in polarization sensitivity of common SNSPDs, see for example [28]), depolarizer transmissivity of 0.847, fiber adapters transmissivity of 0.956, DWDM transmissivity of 0.40(2), and CWDM transmissivity of 0.73, which results in total system detection efficiency of 0.172(9).

Table 1. Approximate values of fused silica attenuation constants for different wavelengths, based on a simplified model from [29].

Wavelength, [nm]	1270	1310	1330	1490	1550
α, [dB/km]	0.34	0.32	0.28	0.19	0.17

To quantify the background noise in quantum channels, we adjust the launching power of the classical transmitters by variable attenuators. We obtain a dependence of BS and FS noise photon rates on input photon rates (calculated from the corresponding input power of the classical signals) in a quantum link of a fixed length with an SNSPD. We distinguish noise contributions from different wavelengths of the input classical signal, and plot these in Fig. 3. These measurements confirm the linear dependence of the noise on input signal power and noise reduction for signals further detuned from the dedicated quantum channel.

Next, we measure background noise generated in the same quantum channel for different lengths of the common fiber at a fixed launching power of 10^{14} photons per second, converted from power measurements. As before, we distinguish the contribution to background noise from the classical signal at different wavelengths; the obtained dependencies of background noise for both FS and BS are shown in Fig. 4. We introduce a theoretical model for noise generation that describes the observed properties of FS and BS. We also derive a system of algebraic equations that allows the extraction of the input/output losses/transmissivities of the fiber links, and then we obtain corresponding corrections to the raw experimental background noise data.

3.3. Background-generation constants

We use Eqs. (2-5) to extract the background-generation constants $\beta^{\mathrm{BS}}_{\lambda_\mathrm{s},\lambda_\mathrm{n}}$ and $\beta^{\mathrm{FS}}_{\lambda_\mathrm{s},\lambda_\mathrm{n}}$ from the experimental data for different signal wavelengths, see Fig. 5 and Table 2. The obtained values show that almost two orders of magnitude noise reduction can be achieved by switching from 1490 nm to 1270 nm synchronization signals. Anomalous high optical loss and background-generation constants in the 12 km fiber spool were consistently observed, as seen in Fig. 5.

This noise measurement in a single DWDM channel can be extended to a significantly wider transmission band. Using a spectrometer, we determine the noise generated from 1500 nm to 1620 nm. To do so, we separately make spectral measurements in 1510 nm, 1530 nm, 1550 nm, 1570 nm, 1590 nm, and 1610 nm CWDM channels as shown in Fig. 6. We normalize spectral data using the data obtained with a single-photon detector for a single DWDM channel. Qualitatively, the noise level seen by the spectrometer is similar (to within one order of magnitude) to that measured in a 1547.72 nm channel. The system efficiency of the spectrometer is nearly a constant in the shown wavelength region. This large transparency window can be sub-divided to more than 100 quantum channels similar to the DWDM channel we used for our measurement. Thus, more than 100 quantum channels can coexist with a single synchronization channel in the

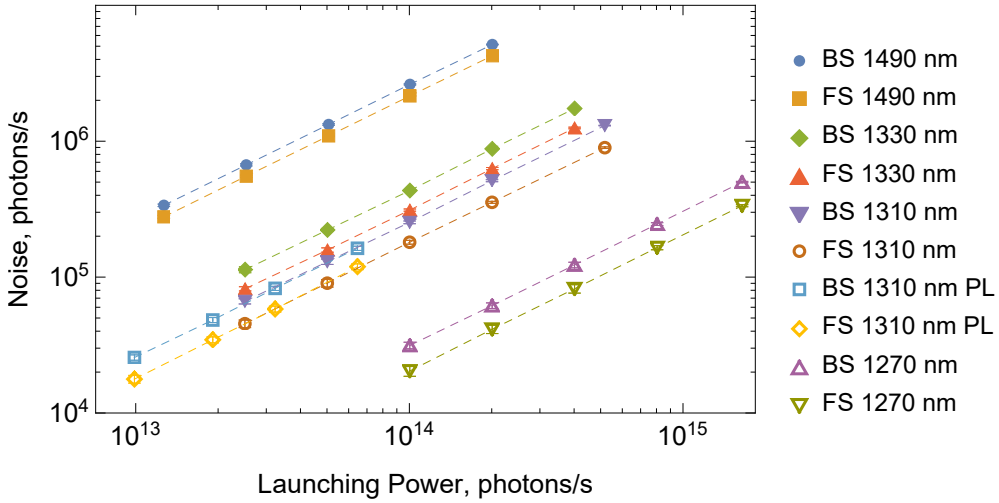

Fig. 3. Background noise photon rate measured at different launching powers (converted into photon count rates) and wavelengths of synchronization transmitters in a single 100 GHz wide DWDM channel of a 25 km fiber link. BS - Counter-propagating or back-scattered noise; FS - co-propagating or forward-scattered noise, PL - marks results obtained with pulsed laser synchronization setup. Error bars correspond to one standard deviation. Dashed lines are guides for an eye. Note: this results was corrected for total system detection efficiency, but was not corrected for terminal losses at fiber ports (i.e. P_{exp} in Eq. (4)).

same fiber.

3.4. Synchronization using off-the-shelf classical components

We now study the background noise generated in common fiber of different lengths for a fixed output power of 1 μW corresponding to a sensitivity of -30 dBm, typically achievable with off-the-shelf classical receivers. Indeed, in our experiments, synchronization was achieved with $\lesssim$ 1 μW with the commercial receiver units. Although we chose 1 μW as a benchmark for classical synchronization, other benchmarks can be computed in a similar way. Below, we obtain the coexistence limit for an arbitrary classical power.

In Fig. 7, we show experimentally measured background noise (shown with plot markers) adjusted for terminal loss of the optical fiber communication links and the expected background from the theoretical model (Eq. 6) using the experimental values of background-generation constants from Table 2. Notice that the experimental data closely follow the theoretical curves, except that for the 12 km spool where the anomaly high loss was observed. Independent study of the spool has revealed a defect in the fiber that may result in coupling of the light into a cladding of the fiber and subsequently result in higher levels of noise generated in the spool [30].

In contrast to Fig. 4, when the output power is fixed there is no saturation of the BS noise because as we increase the fiber length we have to increase the launching power of the synchronization signal. Interestingly, in this case the FS noise can saturate to $P_{\mathrm{out}}\beta^{\mathrm{FS}}_{\lambda_{\mathrm{s}},\lambda_{\mathrm{n}}}/(\alpha_{\mathrm{n}}-\alpha_{\mathrm{s}})$ for long fiber lengths, but only when $\alpha_{\mathrm{n}} > \alpha_{\mathrm{s}}$.

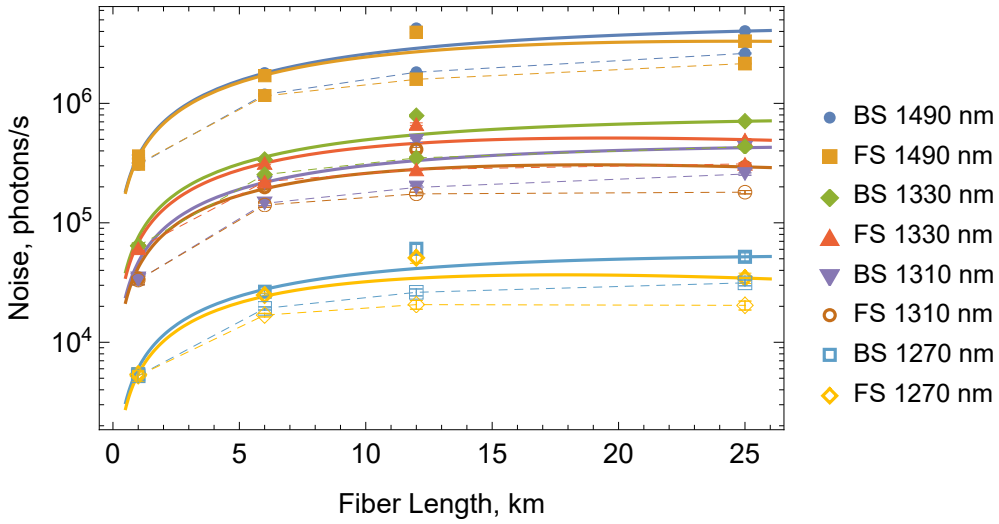

Fig. 4. Background noise photon rate in the single DWDM channel (1547.72 nm) vs. length of the fiber link and wavelengths of synchronization transmitters at a fixed launching power of 10^{14} photons per second. BS - Counter-propagating or back-scattered noise; FS - co-propagating or forward-scattered noise. Error bars are smaller or comparable to plot markers. Plot markers connected with thin dashed lines correspond to raw experimental data (i.e. P_{exp} in Eq. (4)). The second set of plot markers of the same shape and color correspond to the same experimental measurements, but the values are corrected for fiber link terminal losses (i.e. P in Eq. (4)). Both datasets are corrected for the total system detection efficiency. Dashed lines are guides for an eye connecting raw experimental data points. Solid curves are obtained using models described by Eqs. (2) and (3) and coefficients $\beta^{\mathrm{BS}}_{\lambda_s,\lambda_n}$ and $\beta^{\mathrm{FS}}_{\lambda_s,\lambda_n}$ extracted from 25 km link measurements and Eq. (4).

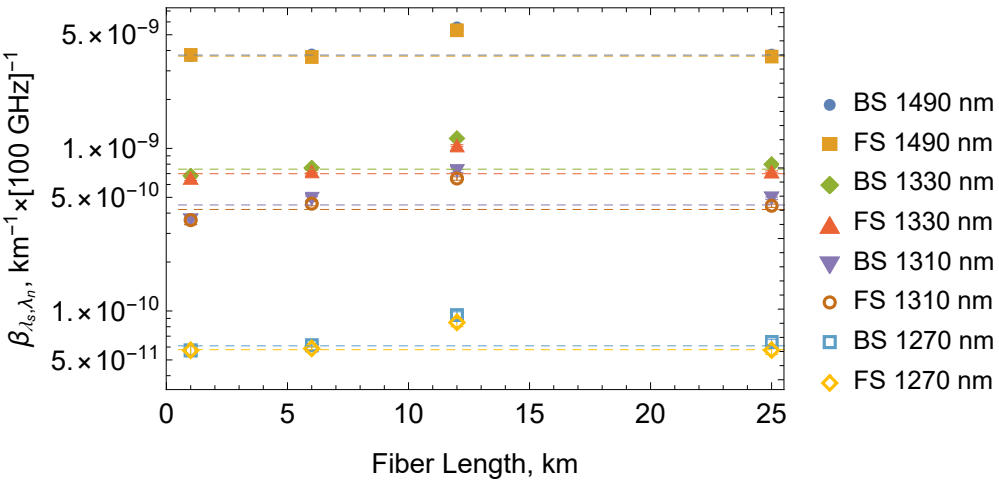

Fig. 5. Background-generation constants $\beta^{\mathrm{BS}}_{\lambda_s,\lambda_n}$ and $\beta^{\mathrm{FS}}_{\lambda_s,\lambda_n}$ for a 100 GHz wide DWDM channel C37 (λ_n = 1547.72 nm) and different signal wavelengths λ_s extracted from the experimental data shown in Fig. 4 using equations (2-5). Dashed lines show mean values for L = 1 km, 6 km, and 25 km.

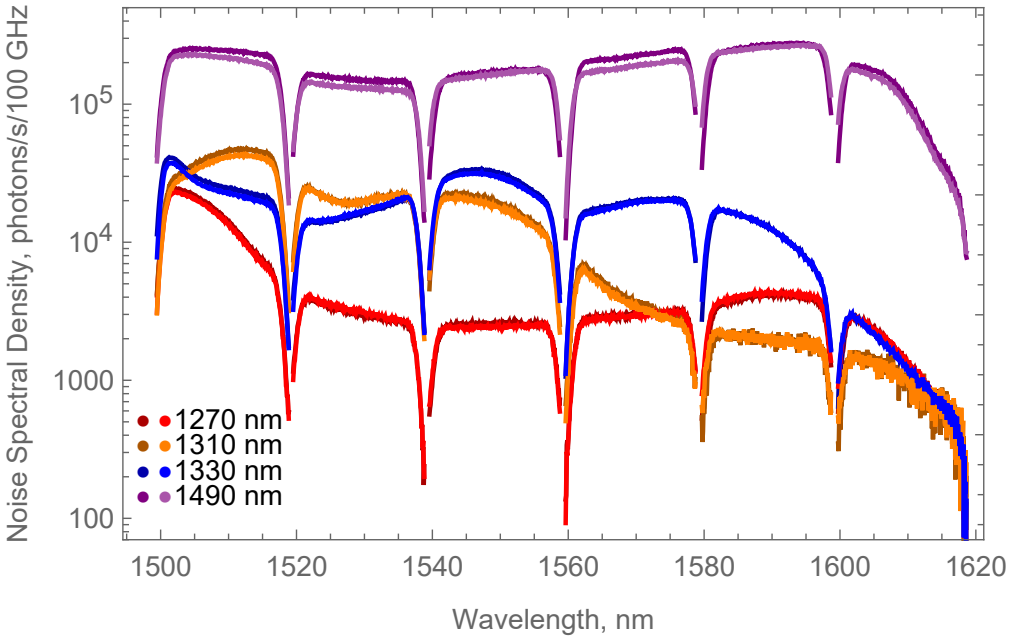

Fig. 6. Relative background noise spectral density normalized by that of a single DWDM channel. The noise is generated in a 6 km fiber by WR transmitters that are attenuated such that 1 μW optical signal power is measured at the WR receiver. Dark curves - BS noise, lighter curves - FS noise. Each background noise spectrum is obtained by consecutive measurements of 20 nm CWDM channels, therefore gaps seen at 1520 nm, 1540 nm,..., 1620 nm are due to edge effects in the CWDM demultiplexer.

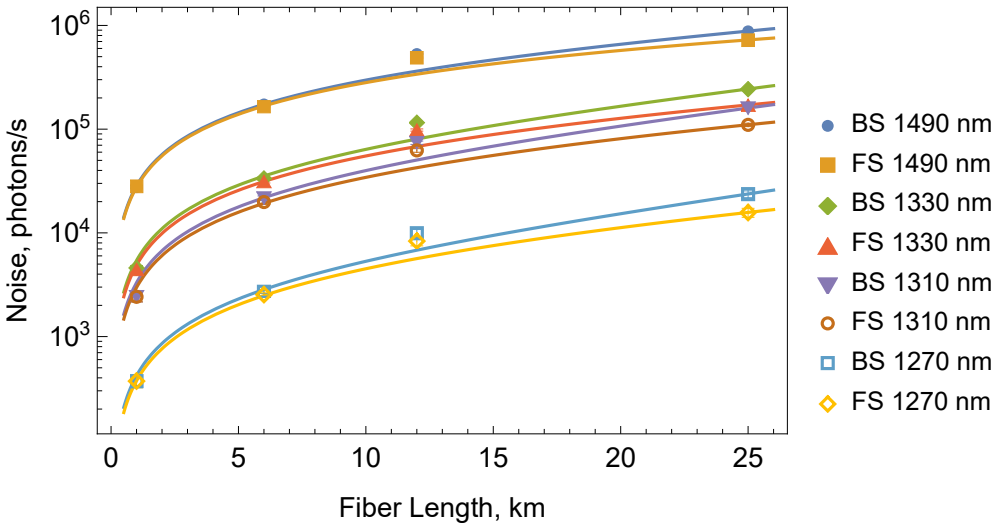

Fig. 7. Measured background noise in 1547.72 nm DWDM channel generated in a common fiber for different fiber lengths at a fixed synchronization signal output power of 1 μW (symbols) and noise figures (solid lines) predicted from theory (Eq. 6 and Table 2). The experimental points are corrected for both total system detection efficiency and terminal losses at the fiber ports (i.e. P_{exp} in Eq. (4)).

Table 2. Background-generation constants $\beta^{BS}_{\lambda_s,1547.72}$ and $\beta^{FS}_{\lambda_s,1547.72}$ in a single 100 GHz DWDM channel for different classical signal wavelengths extracted from the experimental data shown in Fig. 4 using equations (2-5). The background-generation conversion constants in SI units of 10^{-23} $[m \cdot s^{-1}]^{-1}$.

L, [km] / λ, [nm]	1	6	12	25	Mean*
1490 (BS)	3.69(7)	3.78(3)	5.55(4)	3.78(3)	3.75(3)
1490 (FS)	3.76(7)	3.65(3)	5.33(4)	3.67(2)	3.69(3)
1330 (BS)	0.68(2)	0.76(1)	1.15(1)	0.797(7)	0.745(9)
1330 (FS)	0.66(2)	0.72(1)	1.04(1)	0.718(9)	0.699(9)
1310 (BS)	0.36(2)	0.49(1)	0.73(1)	0.494(8)	0.449(9)
1310 (FS)	0.36(2)	0.46(1)	0.65(2)	0.44(1)	0.421(9)
1270 (BS)	0.057(4)	0.062(1)	0.094(5)	0.064(3)	0.061(2)
1270 (FS)	0.057(4)	0.059(1)	0.085(5)	0.057(3)	0.058(2)

*Conversion constants obtained for 12 km fiber link are excluded from the mean values.

3.5. Synchronization performance

Further, we characterize the clock synchronization using WR switches with transceivers operating at two different wavelength pairs and, independently, a pulsed picosecond diode laser. In both cases, a 10 MHz clock output from the GM WR switch, locked to a commercial rubidium clock, is used as a reference. In Fig. 8, we plot the time interval error (TIE) which is $\sqrt{3}$ times larger than time deviation (TDEV) [31]. We use delay measurements from a low-jitter time tagger (1.5 ps RMS timing jitter per channel) to calculate TIE.

The WR measurements were performed with a 1 km fiber spool and the WR signals were attenuated to the lowest power at which the synchronization protocol operates (this power was different for different wavelengths and depends on particular commercial receiver module sensitivity). With the WR setup, we measured a TIE with 1 pulse averaging giving the timing jitter of ≈ 2.18 ps, which is very close to the intrinsic jitter of the time tagger for two channels (2.12 ps RMS). Based on this result, one can conclude that the WR switches provide picosecond level timing jitter for short-timescale synchronization. We observe that the WR is prone to the intrinsic timing drift on a millisecond timescale, i.e. with 10^4 to 10^6 pulses averaged.

Similarly, the synchronization over a 1 km link with a pulsed laser (PL) is tested. Here, the PL is attenuated to the level just above the detection threshold of our system. Measurements of TIE obtained with an off-the-shelf picosecond PL yield a higher single-shot TIE of ≈ 3.5 ps, but this higher timing jitter is most likely due to the signal-to-noise figure intrinsic to the detector. This TIE follows the Gaussian noise averaging trend and can be reduced to 100 fs when $\geq 10^4$ pulses are averaged, equivalent to a 1 ms averaging time.

We were able to synchronize two nodes with fiber lengths up to 18 km using commercial 40 km small form-factor pluggable (SFP) optical network modules operating at 1310 nm and 1490 nm pair of wavelength, and up to 12 km with 10 km SFP modules operating at 1330 nm and 1270 nm pair of wavelength. The TIE plots (not shown) measured for different fiber lengths of 6 km, 12 km, and 18 km for both WR and PL do not reveal significantly different features.

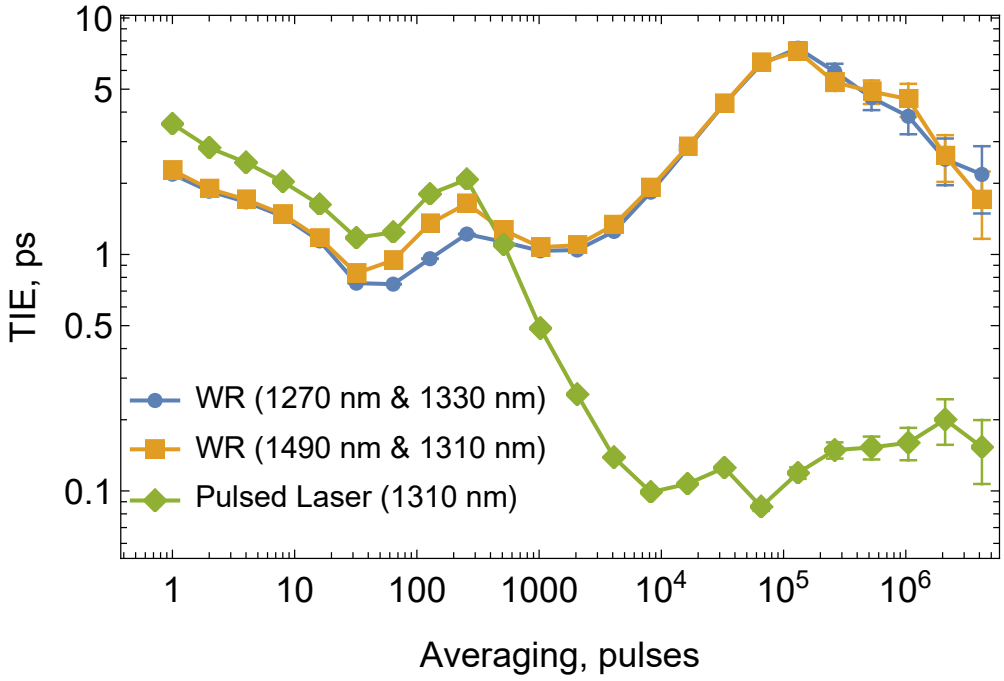

Fig. 8. Allan deviation of timing jitter for WR protocol implemented using optical transceivers operating at 1270 nm and 1330 nm or 1310 nm and 1490 nm wavelength pairs and pulsed laser at 1310 nm with fast detector for 1 km optical fiber channel. The error bars are confidence interval for the Allan deviation estimate.

3.6. Hong-Ou-Mandel interference in the presence of noise and imperfect synchronization

Based on experimentally obtained background generation constants, we can analytically address performance of a distributed Hong-Ou-Mandel measurement in a coexisting network environment. First, we find the indistinguishability of two single photon pulses affected by non-simultaneous arrival of the photons on a beam splitter. The overlap between two Gaussian pulses of width σ (RMS) that are separated by time t can be found analytically: $\exp(-(t^2/(8\sigma^2)))$. The second order coherence $g^{(2)}$ is proportional to the fourth power of the field, therefore the mean indistinguishability can be found by averaging of the squared overlap over a zero-mean normal distribution with the width δt (RMS) due to to the clock synchronization jitter, and in our approximation it has a simple analytical form:

$$I = \int_{-\infty}^{\infty} \left(\int_{-\infty}^{\infty} \frac{e^{-\frac{x^2}{2\sigma^2}}}{\sqrt{2\pi}\sigma} \frac{e^{-\frac{(x-t)^2}{2\sigma^2}}}{\sqrt{2\pi}\sigma} dx \right)^2 \frac{e^{-\frac{t^2}{2\delta t^2}}}{\sqrt{2\pi}\delta \mathrm{t}} dt = \frac{1}{\sqrt{1+\frac{\delta t^2}{2\sigma^2}}}.$$

To include background due to coexisting signals, we write second order coherence between two independent pulsed sources “A” and “B” transmitting single photons and background light via fiber links to the input ports of a 50/50 beamsplitter “a” and “b”. The probability of a detection p_1, p_2 per each trial on detectors “1”, “2” is:

$$p_1 = (p_\mathrm{a} + p_\mathrm{b} + p_\mathrm{a}^\mathrm{n} + p_\mathrm{b}^\mathrm{n})\eta_1/2$$

$$p_2 = (p_\mathrm{a} + p_\mathrm{b} + p_\mathrm{a}^\mathrm{n} + p_\mathrm{b}^\mathrm{n})\eta_2/2,$$

where η_1, η_2 are detection efficiencies of the detectors, and p_a^n, p_b^n are the probabilities to receive a noise photon from fiber links connecting light sources "A" and "B" to beam splitter input ports "a" and "b". Here, we assume that the single photon probabilities are small due to loss in an optical link. Also, the sources are pure, $g^{(2)}_{a,b}(0) = 0$. In addition, we assume that the noise photon probabilities are also small, p_a^n, $p_b^n \ll 1$, which allows us to keep linear terms only. Then, the probability of a coincidence at the detectors 1 and 2 can be written as:

$$p_{12} = \frac{\eta_1\eta_2}{2}\left(p_a p_b(1-I) + p_a p_a^n + p_a p_b^n + p_b p_a^n + p_b p_b^n + p_b^n p_a^n + \frac{(p_a^n)^2}{2} + \frac{(p_b^n)^2}{2}\right).$$

Because probabilities of receiving single photons and noise photons are small, we only keep quadratic terms here. We also take advantage of the Poisson distribution of the noise photons. The last two terms give a probability to receive two noise photons simultaneously. Then, the zero-delay second order coherence can be estimated as $g^{(2)}(0) \approx p_{12}/(p_1 p_2)$ [32].

Before making more general statements, consider a use case of observing non-classical Hong-Ou-Mandel (HOM) interference with two distant indistinguishable single photon sources for pulses with duration of $\sigma \approx 10$ ps. The (heralded) single-photon probability at the source is $p_0 = 1$. The single-photon probabilities are attenuated by fiber propagation loss $p_a = p_b = p_0 e^{-\alpha_{1550} L}$. The results shown here are obtained assuming commercially available 1270 nm/1330 nm classical transmitters that deliver 1 μW to each of the two receivers (see Fig. 7). The probability of the noise photon arrival in the same time gate where a single photon is expected is given by $p_a^n \approx p_b^n = \text{Noise[photons/s]} \times \text{Gate[s]} \ll 1$, where detection gate time Gate $= 2\sigma + \delta t$. Note that a physical implementation of a gate may be critical for long fiber links, because the ungated rate of noise photons can significantly exceed a million (Noise[cps] $>> 10^6$). To address this deficiency, single-photon detectors (SPDs) should be gated with sub-nanosecond gate intervals. Because direct sub-nanosecond gating of single-photon detectors may be difficult [33], electro-optical modulators can be employed to gate the inputs to the SPDs.

In Figure 9, we show the expected value of the $g^{(2)}(0)$ as a function of fiber link length (assuming that links "a" and "b" have the same length) for different clock synchronization time jitter values. The HOM dip is non-classical when $g^{(2)}(0) < 0.5$. At L=0, the $g^{(2)}(0)$ is above zero due to imperfect single-photon overlap (i.e. due to timing jitter). We see that jitter values below 10 ps are not significantly affecting the indistinguishability. For longer L, single photons are increasingly lost due to fiber attenuation; while at the same time, noise due to the classical channel becomes more dominant. We observe that $g^{(2)}(0)$ gets affected at $L > 60$ km, and becomes classical for $L \approx 100$ km.

Although this result is obtained assuming a particular implementation of a quantum network, the methodology can be generalized to all types of single-photon emitters in the quantum network. Indeed, the single-mode states temporal and spectral properties are related through a Fourier transform such that the temporal and spectral widths are inversely proportional. Therefore, narrow spectral filtering of "long" single photons (such as those generated by atoms and ions) can offset the temporal duration of the wave-function to the same degree as fast temporal gating of "short" single photons (such as those generated by parametric down-conversion or four-wave mixing) can offset the spectral bandwidth. In all those cases, the performance of the noise filter is bounded by the same limit due to the time-bandwidth relation required for *indistinguishable* photons.

On the other hand, the limit of ≈100 km is due only to the sensitivity of the off-the shelf classical receivers employed for the WR protocol. Research grade receivers offer significantly better sensitivities. Generally, we can find the theoretical limit of classical/quantum channel coexistence as a function of the classical channel output optical power and the fiber link length by resolving equation $g^{(2)}(0) = 0.5$ for P_{out} as a function of fiber length L for measurement gating

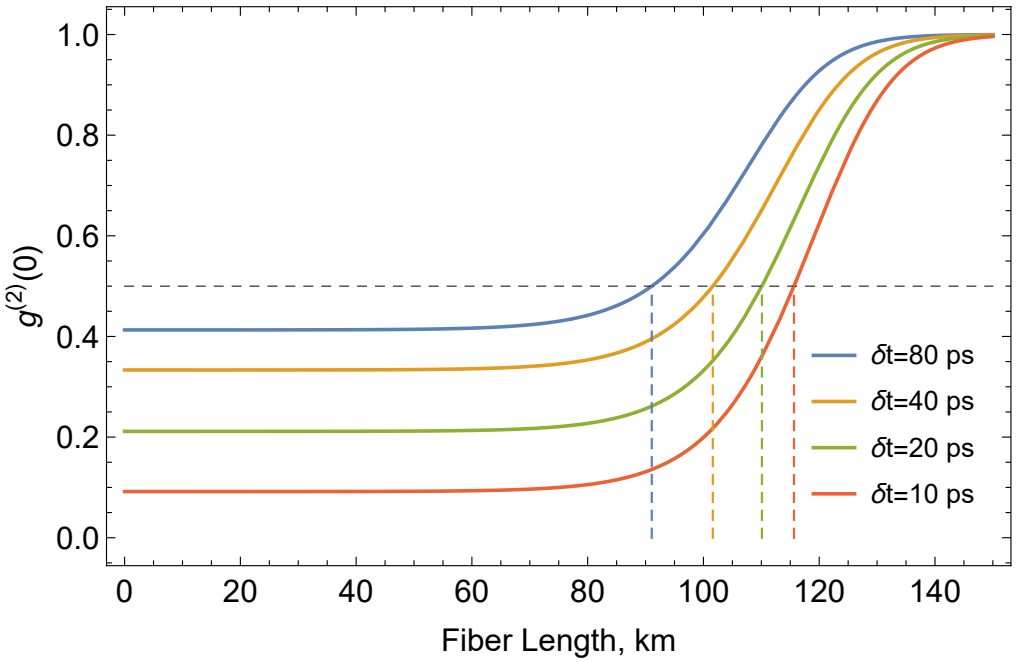

Fig. 9. Zero-delay second order coherence function $g^{(2)}(0)$ as a function of fiber link length. Fiber link length and the 1550 nm single-photon sources are considered identical for each time jitter value. Noise corresponds to the sum of the larger (FS or BS) noise produced by both 1270 nm and 1330 nm classical synchronization pulses. Gating time is given by the sum of pulse width and time jitter: $2\sigma + \delta t$.

time of T_{gate}:

$$P_{\text{out}}(L) = (T_{\text{gate}})^{-1} \frac{\left(\sqrt{I+1}-1\right)(\alpha_{\lambda_1}+\alpha_{\lambda_n})(\alpha_{\lambda_2}+\alpha_{\lambda_n})e^{-\alpha_{\lambda_n}L}}{\beta^{\text{BS}}_{\lambda_1,\lambda_n}(\alpha_{\lambda_2}+\alpha_{\lambda_n})e^{\alpha_{\lambda_1}L}+\beta^{\text{BS}}_{\lambda_2,\lambda_n}(\alpha_{\lambda_1}+\alpha_{\lambda_n})e^{\alpha_{\lambda_2}L}}. \tag{7}$$

This simple form of the limit (7) can be obtained if both photons travel through the fiber links of the same length and $L >> 1$ km and using BS noise for both classical wavelengths to obtain a stricter bound. In Fig. 10, the limit is plotted for $\lambda_1 = 1270$ nm, $\lambda_2 = 1330$ nm and a single DWDM channel at $\lambda_n = 1550$ nm, for unit indistinguishability $I = 1$ and Fourier-transform-limited gating corresponding to zero time jitter and dispersion compensated fiber propagation in a single DWDM channel: $T_{\text{gate}} = [100\ GHz]^{-1} = 10$ ps. Note that this absolute limit is established as a function of power in the classical channel, not the data rate. Nonetheless, some useful estimations can be made.

The physical limit on the receiver sensitivity is given by the Shannon limit for receivers based on a classical measurement and by the Holevo bound for receivers based on a quantum measurement [34–36]. Although different implementations of receivers are possible, we estimate that coherent states with the average energy of 1 photon at the receiver are required to communicate one bit of classical information, which amounts an optical power reduction of to up to 8 orders of magnitude for the signal at the receiver using the same synchronization protocol as compared to off-the-shelf receivers. A typical WR-PTP setup requires a data rate of <100 kilobits per second, [37]. As we see from the plot, with our assumptions on a receiver for classical information, the WR protocol puts a limit on the length of the quantum link at ≈ 300 km. Even though there is no hard theoretical limit for the length of a fiber link as a function of classical data rate, stretching

beyond 400 km would be unfeasible, because at that point the classical signal at the output of the fiber link will be attenuated to below one photon per second.

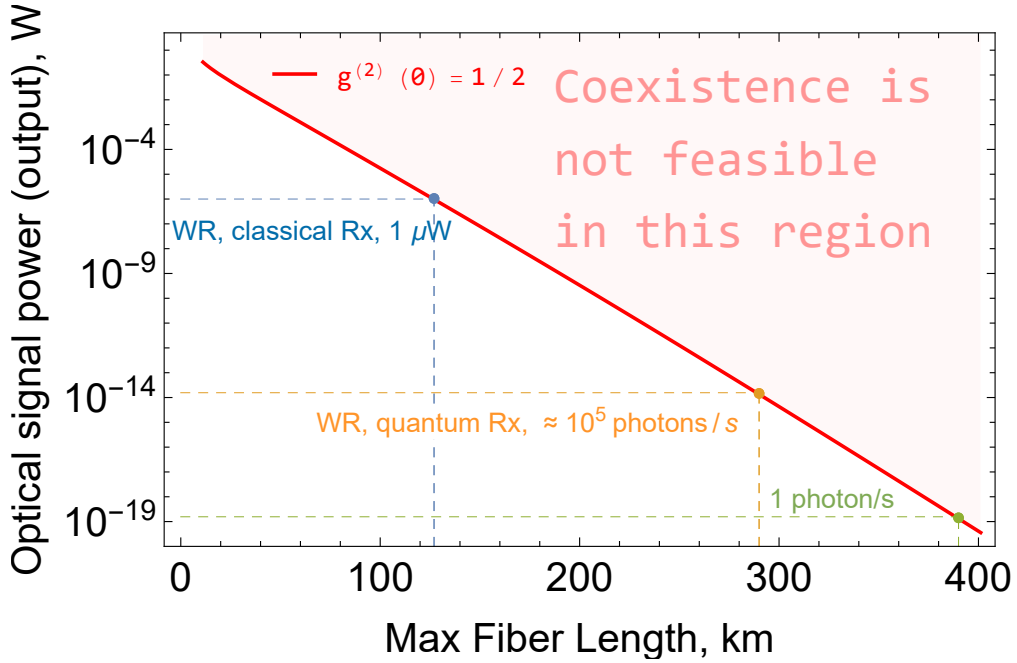

Fig. 10. Classical and quantum coexistence limit as a function of fiber link length and the output optical power of the classical signal ($g^{(2)}(0) = 0.5$, red line) assuming synchronization with negligible timing jitter ($\ll$10 ps). The area shaded with light red shows the parameter space where the coexistence of quantum and classical channels is not feasible. Also shown are notable use cases. When the synchronization with off-the-shelf components and WR PTP protocol output optical power of $\approx$1 μW is required, the maximum length of the fiber link is $\approx$100 km for the idealized quantum source with unit heralding efficiency (blue dashed lines). With quantum receivers operating near their measurement limit, the power requirements drop 8 orders of magnitude and the extension of the fiber link to about 300 km is possible (yellow dashed lines). Although there is no fundamental limit on the optical power at the receiver in a classical channel, the extension of coexisting links over 400 km is unfeasible, because the classical power of 1 photon per second at the receiver sets the practical limit for any useful synchronization protocol (green dashed lines).

4. Conclusion

In this work, we have built a time-synchronized quantum network testbed and shown that classical synchronization pulses can in principle coexist with single-photon quantum channels in the same optical fiber. The duration of single-mode single-photons does not play a role as far as coexistence is concerned, but may be important given limits on synchronization. We demonstrate a successful synchronization of the 2 quantum nodes and achieve a timing jitter $<$ 2.2 ps RMS with WR switches and $<$ 3.5 ps with picosecond PL. We show that frequency stabilization $<$ 100 fs RMS can in principle be achieved with a PL via averaging synchronization pulses over $\approx$1 ms.

We have shown that background noise generated by bright synchronization signals can be kept low by detuning the carrier frequency of classical signals to (or below) 1300 nm. In this configuration, a sizable band (1500 nm to 1620 nm) can be used to multiplex more than

100 quantum channels. As we have shown, the synchronization achieved between the two nodes and the background induced by a classical synchronization protocol with off-the-shelf components is theoretically sufficient to achieve quantum HOM interference visibilities i.e. even classically-synchronized nodes are compatible with the coexistent distribution of non-classical states. When using off-the-shelf components, the power requirement at the receiver is typically -30 dBm (1 μW), which is significantly above the fundamental limit (Helstrom bound, [38]). We determine the maximal achievable fiber lengths supporting coexistence for (1) current state of the art classical equipment and (2) the future quantum-enabled classical data exchange protocols. When using off-the-shelf components, the power requirement at the receiver limits the fiber lengths to $\approx$ 100 km whereas a receiver operating close to the fundamental limit improves that fiber length more than twofold. Interestingly, the maximal practical length of many quantum network protocols without repeaters is limited by $\approx$100 km anyway due to fiber loss only. Here, we have shown that the maximal length of coexisting fiber links is not significantly different and can be improved. Thus, the limited use of fiber dedicated to quantum communication to also exchange classical information, which can significantly simplify the architecture of the quantum network, is fundamentally possible.

Acknowledgments

The authors thank Alan Mink, Krister L. Shalm, and Joshua Bienfang for fruitful discussions and for proofreading the draft of the manuscript.

Disclosures

The authors declare no conflicts of interest.

Data availability

Data underlying the results presented in this paper are not publicly available at this time but may be obtained from the authors upon reasonable request.

References

1. J. C. Bienfang, A. J. Gross, A. Mink, B. J. Hershman, A. Nakassis, X. Tang, R. Lu, D. H. Su, C. W. Clark, C. J. Williams, E. W. Hagley, and J. Wen, "Quantum key distribution with 1.25 gbps clock synchronization," Optics Express **12**, 2011–2016 (2004).
2. J. I. Cirac, P. Zoller, H. J. Kimble, and H. Mabuchi, "Quantum state transfer and entanglement distribution among distant nodes in a quantum network," Physical Review Letters **78**, 3221 (1997).
3. B. Ndagano and A. Forbes, "Entanglement distillation by hong-ou-mandel interference with orbital angular momentum states," APL Photonics **4**, 016103 (2019).
4. Y. Chen, S. Ecker, S. Wengerowsky, L. Bulla, S. K. Joshi, F. Steinlechner, and R. Ursin, "Polarization entanglement by time-reversed hong-ou-mandel interference," Physical Review Letters **121**, 200502 (2018).
5. M. Zukowski, A. Zeilinger, M. A. Horne, and A. K. Ekert, "" event-ready-detectors" bell experiment via entanglement swapping." Physical Review Letters **71** (1993).
6. R.-B. Jin, M. Takeoka, U. Takagi, R. Shimizu, and M. Sasaki, "Highly efficient entanglement swapping and teleportation at telecom wavelength," Scientific reports **5**, 1–7 (2015).
7. J.-W. Pan, D. Bouwmeester, H. Weinfurter, and A. Zeilinger, "Experimental entanglement swapping: entangling photons that never interacted," Physical review letters **80**, 3891 (1998).
8. P. Aboussouan, O. Alibart, D. B. Ostrowsky, P. Baldi, and S. Tanzilli, "High-visibility two-photon interference at a telecom wavelength using picosecond-regime separated sources," Phys. Rev. A **81**, 021801 (2010).
9. S.-B. Cho and T.-G. Noh, "Stabilization of a long-armed fiber-optic single-photon interferometer," Opt. Express **17**, 19027–19032 (2009).
10. T. van Leent, M. Bock, R. Garthoff, K. Redeker, W. Zhang, T. Bauer, W. Rosenfeld, C. Becher, and H. Weinfurter, "Long-distance distribution of atom-photon entanglement at telecom wavelength," Phys. Rev. Lett. **124**, 010510 (2020).
11. H. de Riedmatten, I. Marcikic, J. A. W. van Houwelingen, W. Tittel, H. Zbinden, and N. Gisin, "Long-distance entanglement swapping with photons from separated sources," Phys. Rev. A **71**, 050302 (2005).

12. Q.-C. Sun, Y.-F. Jiang, Y.-L. Mao, L.-X. You, W. Zhang, W.-J. Zhang, X. Jiang, T.-Y. Chen, H. Li, Y.-D. Huang, X.-F. Chen, Z. Wang, J. Fan, Q. Zhang, and J.-W. Pan, "Entanglement swapping over 100 km optical fiber with independent entangled photon-pair sources," Optica **4**, 1214–1218 (2017).
13. M. Alshowkan, B. P. Williams, P. G. Evans, N. S. Rao, E. M. Simmerman, H.-H. Lu, N. B. Lingaraju, A. M. Weiner, C. E. Marvinney, Y.-Y. Pai, B. J. Lawrie, N. A. Peters, and J. M. Lukens, "Reconfigurable quantum local area network over deployed fiber," PRX Quantum **2**, 040304 (2021).
14. M. Alshowkan, P. G. Evans, B. P. Williams, N. S. V. Rao, C. E. Marvinney, Y.-Y. Pai, B. J. Lawrie, N. A. Peters, and J. M. Lukens, "Advanced architectures for high-performance quantum networking," (2021).
15. M. Lipiński, T. Włostowski, J. Serrano, and P. Alvarez, "White rabbit: a ptp application for robust sub-nanosecond synchronization," in "2011 IEEE International Symposium on Precision Clock Synchronization for Measurement, Control and Communication," (2011), pp. 25–30.
16. M. Rizzi, M. Lipinski, P. Ferrari, S. Rinaldi, and A. Flammini, "White rabbit clock synchronization: Ultimate limits on close-in phase noise and short-term stability due to fpga implementation," IEEE Transactions on Ultrasonics, Ferroelectrics, and Frequency Control **65**, 1726–1737 (2018).
17. "Ieee standard for a precision clock synchronization protocol for networked measurement and control systems," IEEE Std 1588-2019 (Revision ofIEEE Std 1588-2008) pp. 1–499 (2020).
18. Commercial equipment and software referred to in this work is identified for informational purposes only, and does not imply recommendation of or endorsement by the National Institute of Standards and Technology, nor does it imply that the products so identified are necessarily the best available for the purpose.
19. N. A. Peters, P. Toliver, T. E. Chapuran, R. J. Runser, S. R. McNown, C. G. Peterson, D. Rosenberg, N. Dallmann, R. J. Hughes, K. P. McCabe, J. E. Nordholt, and K. T. Tyagi, "Dense wavelength multiplexing of 1550 nm qkd with strong classical channels in reconfigurable networking environments," New Journal of physics **11**, 045012 (2009).
20. P. D. Townsend, "Simultaneous quantum cryptographic key distribution and conventional data transmission over installed fibre using wavelength-division multiplexing," Electronics Letters **33**, 188–190 (1997).
21. T. E. Chapuran, P. Toliver, N. A. Peters, J. Jackel, M. S. Goodman, R. J. Runser, S. R. McNown, N. Dallmann, R. J. Hughes, K. P. McCabe, J. E. Nordholt, C. G. Peterson, K. T. Tyagi, L. Mercer, and H. Dardy, "Optical networking for quantum key distribution and quantum communications," New Journal of Physics **11**, 105001 (2009).
22. K. Patel, J. Dynes, I. Choi, A. Sharpe, A. Dixon, Z. Yuan, R. Penty, and A. Shields, "Coexistence of high-bit-rate quantum key distribution and data on optical fiber," Physical Review X **2**, 041010 (2012).
23. C. Liang, K. F. Lee, J. Chen, and P. Kumar, "Distribution of fiber-generated polarization entangled photon-pairs over 100 km of standard fiber in oc-192 wdm environment," in "2006 Optical Fiber Communication Conference and the National Fiber Optic Engineers Conference," (2006), pp. 1–3.
24. J. M. Thomas, G. S. Kanter, E. M. Eastman, K. F. Lee, and P. Kumar, "Entanglement distribution in installed fiber with coexisting classical light for quantum network applications," in "Optical Fiber Communication Conference (OFC) 2022," (Optica Publishing Group, 2022), p. Tu3I.3.
25. Certain commercial equipment and software used to implement White Rabbit extension to the IEEE 1588-2008 precision time protocol [17] (WRPTP) is referred in this manuscript as White Rabbit or WR equipment, software or protocol.
26. White Rabbit logo is intellectual property of CERN. The logo is licensed under "Attribution-ShareAlike 4.0 International (CC BY-SA 4.0)" https://creativecommons.org/licenses/by-sa/4.0/. The logo authored by Alexandra Lewis.
27. We use the substitution method with calibrated attenuators to find the detection efficiency of the SNSPD. First, we calibrated two optical attenuators. We employ a classical InGaAs photodiode to determine the attenuation factor of the attenuators. We have measured attenuation factors of 9010(40) and 935(7). Where the uncertainty was estimated as a statistical uncertainty of one standard deviation. Then, we measured the optical power of a laser beam with the fiber-coupled calibrated InGaAs photodiode using a trans-impedance amplifier. The InGaAs photodiode specified detection efficiency was 0.805(1), the transmittance of the InGaAs photodiode coupler was 0.953(3), and the gain of the trans-impedance amplifier was set to 10^7 V/A. Then, the optical input to the classical photodiode through a fiber polarization controller (FPC) was attenuated with the calibrated attenuators and the photodiode is substituted with the fiber-coupled SNSPD. The polarization of the laser light was optimized to maximize the photon count rate at the SNSPD detector using the FPC. The output power measured using the InGaAs detector is converted to the average photon rate using the energy of photons at 1550 nm and compared with the measured average photon counting rate from the SNSPD. The ratio between the measured photon rate and the converted input average photon rate was used to determine the detection efficiency of the SNSPD. We repeated the same measurement for three different laser powers and obtained an average detection efficiency of 0.957(5). The maximal contribution to this uncertainty is the statistical uncertainty of calibrating the attenuators and does not include any systematic uncertainty.
28. E. A. Dauler, M. E. Grein, A. J. Kerman, F. Marsili, S. Miki, S. W. Nam, M. D. Shaw, H. Terai, V. B. Verma, and T. Yamashita, "Review of superconducting nanowire single-photon detector system design options and demonstrated performance," Optical Engineering **53**, 081907 (2014).
29. W. Heitmann and K.-F. Klein, "Infrared absorption of silica fibers," Journal of Optical Communications **25**, 106–109 (2004).
30. A. Rahmouni, S. Saha, O. Slattery, and T. Gerrits, "Hyperspectral photon-counting optical time domain reflectometry," in "Quantum Communications and Quantum Imaging XX," , vol. 12238 K. S. Deacon and R. E. Meyers, eds.,

International Society for Optics and Photonics (SPIE, 2022), vol. 12238, p. 1223805.
31. W. Riley and D. Howe, "Handbook of frequency stability analysis," https://tsapps.nist.gov/publication/get_pdf.cfm?pub_id=50505 (2008).
32. A. Migdall, S. V. Polyakov, J. Fan, and J. C. Bienfang, *Single-photon generation and detection: physics and applications* (Academic Press, 2013).
33. M. A. Wayne, J. C. Bienfang, and A. L. Migdall, "Low-noise photon counting above 100× 106 counts per second with a high-efficiency reach-through single-photon avalanche diode system," Applied physics letters **118**, 134002 (2021).
34. I. A. Burenkov, O. V. Tikhonova, and S. V. Polyakov, "Quantum receiver for large alphabet communication," Optica **5**, 227–232 (2018).
35. I. Burenkov, M. Jabir, A. Battou, and S. Polyakov, "Time-resolving quantum measurement enables energy-efficient, large-alphabet communication," PRX Quantum **1**, 010308 (2020).
36. I. A. Burenkov, M. V. Jabir, and S. V. Polyakov, "Practical quantum-enhanced receivers for classical communication," AVS Quantum Science **3**, 025301 (2021).
37. "White rabbit syncronization protocol specification," https://ohwr.org/project/wr-std/wikis/Documents/White-Rabbit-Specification-(latest-version).
38. C. W. Helstrom, "Quantum detection and estimation theory," J. Stat. Phys. **1**, 231–252 (1969).